The Economic Geography of Global Warming

Online Appendix

JOSÉ-LUIS CRUZ
University of California, Berkeley
and
ESTEBAN ROSSI-HANSBERG
University of Chicago

TABLE 3
Summary of parametrization.

1. Energy: $q_t^\omega(r)=\phi_t^\omega(r)^{\gamma_1} z_t^\omega(r)\left(L_t^\omega(r)^\chi e_t^\omega(r)^{1-\chi}\right)^\mu$, $e_t^\omega(r)=\left(\kappa e_t^{f,\omega}(r)^{\frac{\epsilon-1}{\epsilon}}+(1-\kappa)e_t^{c,\omega}(r)^{\frac{\epsilon-1}{\epsilon}}\right)^{\frac{\epsilon}{\epsilon-1}}$ $\mathcal{Q}_t^f(r)=f(CumCO2_t)/\zeta_t^f(r)$, $\mathcal{Q}_t^c(r)=1/\zeta_t^c(r)$, $\zeta_t^j(r)=\left(y_t^w/y_{t-1}^w\right)^{\upsilon^j}\zeta_{t-1}^j(r)$	
$\chi=0.96$	Share of labor in labor-energy composite
$\epsilon=1.6$	Elasticity of substitution between energy sources (Popp, 2004)
$\text{std}(\epsilon)=0.56$	Standard deviation of elasticity of substitution between energy sources (Papageorgiou et al., 2017)
$\kappa=0.89$	Share of fossil fuels in energy composite
$f(\cdot)$	Extraction costs (Rogner, 1997; Bauer et al., 2017)
$\zeta_0^f(\cdot),\zeta_0^c(\cdot)$	Initial energy productivities based on current energy use
$\upsilon^f=1.16$	Elasticity of fossil fuel productivity growth to global real GDP per capita growth
$\upsilon^c=1.22$	Elasticity of clean energy productivity growth to global real GDP per capita growth
2. Damage functions: $\Lambda_t^a(r)=\Lambda^a(\Delta T_t(r),T_t(r))$, $\Lambda_t^b(r)=\Lambda^b(\Delta T_t(r),T_t(r))$, $n_t(r)=\eta(y_t(r),L_t(r))$	
$\Lambda^a(\cdot),\Lambda^b(\cdot)$	Relation between temperature and fundamental productivities and amenities
$\eta(\cdot)$	Relation between natality rates, real GDP, and temperature
3. Carbon cycle and climate	
$g(\cdot)$	Relation between global temperature and local temperature (Statistical down-scaling)
4. Preferences: $\sum_t \beta^t u_t(r)$, $u_t(r)=\left(1+\Lambda_t^b(r)\right)\bar{b}_{t-1}(r)L_t(r)^{-\lambda}\left[\int_0^1 c_t^\omega(r)^\rho \mathrm{d}\omega\right]^{\sigma/\rho}$, $u_0(r)=\mathrm{e}^{HDI_0(r)^3/\psi}$	
$\beta=0.965$	Discount factor
$\sigma=1$	Elasticity of utility to real income
$\rho=0.75$	Elasticity of substitution of 4 (Bernard et al., 2003)
$\lambda=0.32$	Elasticity of amenities to population density (Desmet et al., 2018)
$\Omega=0.5$	Inverse of elasticity of migration flows to income (Monte et al., 2018)
$\psi=0.05$	Relation between utility and HDI (Kummu et al., 2018)
5. Technology: $q_t^\omega(r)=\phi_t^\omega(r)^{\gamma_1} z_t^\omega(r)\left(L_t^\omega(r)^\chi e_t^\omega(r)^{1-\chi}\right)^\mu$, $F^\omega(z,a)=\mathrm{e}^{a_t^\omega(r) z^{-\theta}}$, $a_t(r)=\bar{a}_t(r)L_t(r)^\alpha$	
$\alpha=0.06$	Static elasticity of productivity to density (Carlino et al., 2007)
$\theta=6.5$	Trade elasticity (Eaton and Kortum, 2002; Simonovska and Waugh, 2014)
$\mu=0.8$	Share of non-land in production (Greenwood et al., 1997; Desmet and Rappaport, 2017)
$\gamma_1=0.319$	Relation between population distribution and growth (Desmet et al., 2018)
6. Productivity evolution: $\bar{a}_t(r)=(1+\Lambda_t^a(r))\left(\phi_{t-1}(r)^{\theta\gamma_1}\left[\int_S \bar{a}_{t-1}(v)\mathrm{d}v\right]^{1-\gamma_2}\bar{a}_{t-1}(r)^{\gamma_2}\right)$, $\varphi(\phi)=\nu\phi^\xi$	
$\gamma_2=0.993$	Relation between population distribution and growth (Desmet et al., 2018)
$\xi=125$	Elasticity of bid rents to investments in technology (Desmet and Rossi-Hansberg, 2015)
$\nu=0.15$	Level of innovation costs that yields an initial growth rate of real GDP of 1.75%
7. Trade costs	
$\varsigma(\cdot,\cdot)$	Trade costs computed as in (Allen and Arkolakis, 2014) using the Fast Marching Algorithm
8. Migration costs	
$m_2(\cdot)$	Migration costs to match local population change between 2000 and 2005

A. PARAMETERS AND DATA

Table 3 summarizes the parameters we use in the baseline scenario. The rest of this section discusses the sources and construction of our data.

Population and GDP at $1^\circ\times1^\circ$. Data on population and GDP, in Power Purchasing Parities, for $1^\circ\times1^\circ$ cells across the entire world come from the G-Econ 4.0 research project (Nordhaus, 2006; Nordhaus and Chen, 2016). For the estimation of fundamental amenities and productivities, we use data for the years 1990, 1995, 2000, and 2005. We consider the same 17,048 cells that in 2000 have positive population, GDP and land. If some of these cells display missing values for 1990, 1995 or 2005, we linearly extrapolate the missing data, and, in each period, we cap GDP per capita at the percentile 97.13.

Human Development Index at $1^\circ\times1^\circ$. Kummu et al. (2018) provides data on the Human Development Index at a yearly frequency, from 1990 to 2015, at a sub-national level, considering around 700 geographic units. This data is presented at a resolution

of 5 arc-min, so we aggregate it at a resolution of 60 minutes by considering the mode across cells.

Geographical attributes at $1^\circ \times 1^\circ$. Elevation data, measured as meters above the sea level at a resolution of $1^\circ \times 1^\circ$, is taken from (SIO, 1977) (http://research.jisao.washington.edu/data_sets/elevation/). To construct the standard deviation and the mean absolute error, also known as *roughness*, within each $1^\circ \times 1^\circ$ cell, we use the aforementioned dataset at a resolution of $0.25^\circ \times 0.25^\circ$ and compute these statistics over the cells with positive land. Distance to the coast is taken from the NASA Ocean Biology Processing Group (NASA, 2009) (https://oceancolor.gsfc.nasa.gov/docs/distfromcoast/). This data is provided at a resolution of $0.1^\circ \times 0.1^\circ$, so we compute the average distance within each $1^\circ \times 1^\circ$ cell. Distance to non-frozen oceans at $1^\circ \times 1^\circ$ is taken from the G-Econ database. Distance to nearest water body either inland or sealand (ice-covered land areas are not considered as water bodies) at $1^\circ \times 1^\circ$ is taken from Carrea et al. (2015). The following data are obtained from the NASA Earth Observations (NASA, 2023) (https://neo.sci.gsfc.nasa.gov) at $1^\circ \times 1^\circ$: vegetation density is taken as the average over the period 1951-1980;[1] share of ice-covered land is taken over April of 2010; albedo, which is the ratio of light that a surface reflects compared to the total sunlight that falls, is taken over April of 2010;[2] land cover classification considers the year 2010.[3]

Land density at $1^\circ \times 1^\circ$. Data on land comes from the Global Land One-km Base Elevation (Hastings et al., 1999) Digital Elevation Model, a raster elevation data set from the National Oceanic and Atmospheric Administration covering all $30'' \times 30''$ (arcsecond) cells located on land. Using this information, we compute for each $1^\circ \times 1^\circ$ cell on the globe the share of the $30'' \times 30''$ cells that are on land. Since the size of a $1^\circ \times 1^\circ$ cell is larger in the Equator than in the poles, we adjust the land density by the size of each cell. Finally, we normalize this measure, so that the cell with the largest amount of land has a land density of one.

Temperature at $1^\circ \times 1^\circ$. Gridded temperature data comes from the Berkeley Earth Surface Temperature (Rohde and Hausfather, 2020) (http://berkeleyearth.org/data-new/). This dataset provides information as far as 1750, as frequent as daily maximum, minimum and average temperature and as fine as $0.25^\circ \times 0.25^\circ$. We employ the database that provides annual temperature at a resolution of $1^\circ \times 1^\circ$. For the cells with missing temperature, we take the simple average temperature across the eight surrounding cells, that is, we create a block of cells of size 3×3 centered at the cell with missing data. If there are still cells with missing temperature (occurring for small islands), we create a block of cells of size 5×5 centered at the cell with missing data and take the simple average temperature. We continue with this procedure until the cell is filled with temperature data.

Historical CO_2 *emissions and clean energy at country-level.* Crippa et al. (2019) (https://edgar.jrc.ec.europa.eu/overview.php?v=booklet2020) provides

1. The vegetation index ranges from -0.1 to 0.9 and have no unit. Rather, they are index values in which higher values (0.4 to 0.9) show lands covered by green, leafy vegetation and lower values (0 to 0.4) show lands where there is little or no vegetation.

2. Surfaces that reflect a large share of the light falling on them are bright, and have high albedo, like snow. Surfaces that do not reflect much light are dark, and have low albedo, like forests.

3. This dataset partitions land based on characteristics of the surface that satellites can detect, such as water, soil, and vegetation types. There are 17 categories of land cover: 9 classes of natural vegetation, 3 classes of developed lands, 2 classes of mosaic lands, and 3 classes of non-vegetated lands (snow/ice, bare soil/rocks, water).

CO_2 emissions for all countries considered in this analysis, except for Greenland. We supplement this observation with data from the World Bank. Since Crippa et al. (2019) considers international marine and international aviation, we split those emissions across countries according to the distribution provided in IEA (2020).[4] As for the use of clean energy (expressed in tons of oil equivalent), we use information from BP (2019) and define it as the sum of nuclear, hydroelectricity and renewables (wind, solar, among others). Since this database provides information for some aggregate regions, like Other South America and Other Middle East, we partition the energy use of those aggregate regions across countries according to the pattern for CO_2 emissions presented in Crippa et al. (2019). To make comparable CO_2 emissions and clean energy, we take the ratio of tons of CO_2 per ton of oil equivalent to be 2.8466.

CO_2 emissions and clean energy at $1^\circ \times 1^\circ$. The Emission Database for Global Atmospheric Research (EDGAR, Crippa et al., 2019) version 4.0 (`https://jeodpp.jrc.ec.europa.eu/ftp/jrc-opendata/EDGAR/datasets/v40/`) contains global emission inventories for greenhouse gases and air pollutants. These emissions are calculated as totals by country from 1970 to 2008, and distributed at a resolution of $0.1^\circ \times 0.1^\circ$ using proxy data. We aggregate this data at $1^\circ \times 1^\circ$ by considering the sum across cells. We employ the CO_2 distribution from residential emissions.[5] In order to define carbon dioxide emissions at the cell-level, we disaggregate the country-level emissions according to the spatial pattern displayed in the EDGAR database. As no gridded data for clean energy exists, we split the country-level clean energy use using the spatial pattern of the EDGAR database.[6]

Historical net natality at country-level. Crude birth rates and crude death rates at the country-level since 1950 at a yearly frequency are taken from UN (2019) (`https://population.un.org/wpp/Download/Standard/Population/`).

Projections of non-fuel combustion CO_2 emissions and non-CO_2 forcing. Forecasts up to 2500 for CO_2 flow and forcing for RCP 8.5, 6.0, 4.5 and 2.6 are taken from the RCP Database version 2.0 (Riahi et al., 2007; Fujino et al., 2006; Yasuaki et al., 2008) (`https://tntcat.iiasa.ac.at/RcpDb/dsd?Action=htmlpage&page=welcome`). Carbon dioxide from deforestation is considered as *OtherCO2* and we consider that 1 GtC equals 44/12 $GtCO_2$. Non-CO_2 forcing is considered as *Total anthropogenic and natural radiative forcing* minus *CO2 forcing*.

Projections of global population. Global population levels at a quinquenial frequency for the medium scenario, as well as 80% and 95% confidence intervals are taken from UN (2019) (`https://population.un.org/wpp/Download/Standard/Population/`). In order to make consistent total population from United Nations and G-Econ in the year 2000, from the former dataset we subtract the total population of the initial period and add the total population of the year 2000 displayed in the G-Econ database.[7]

4. Since IEA (2020) provides information for aggregate regions that comprise several countries, like Former Soviet Union or Other Africa, we partition the emissions of those aggregate regions across countries according to the pattern displayed in Crippa et al. (2019) for total emissions.

5. We prefer this specification over total emissions or emissions from production, because the former considers emissions that occur over cells with no land and the latter displays high level of CO_2 in cells scarcely populated and with low income levels (due to the presence of plants producing steel or cement, for instance), and such pattern might not represent the long-run trend of CO_2 emissions.

6. Figure 95 in Supplementary Materials Section O.1 displays the spatial distribution of CO_2 emissions and clean energy in 2000.

7. This adjustment is performed since the G-Econ database does not display information for some regions of the world, like Libya and some parts of Africa and Asia.

Cost of extracting fossil fuels. Bauer et al. (2017) estimates the cost of extracting fossil fuels and present estimates for different Shared Socioeconomics Pathways (SSP), which consider alternative assumption regarding the evolution of the world economy. We choose the scenario SSP5 (development based on fossil fuels), which is the one that closest resembles the RCP 8.5. Then, we aggregate the costs of hard coal and lignite into a single fossil fuel in terms of tCO_2 per usd, considering the conversion factors of 0.0946 and 0.1012 $GtCO_2$ per EJ, respectively. Finally, we rank costs from the least to the most expensive.

Share of agriculture in value added. Conte et al. (2021) estimates the distribution of agricultural output across grid cells by employing data on total crop production from IIASA and FAO (2012).

B. DAMAGE FUNCTIONS ON AMENITIES AND PRODUCTIVITIES

In this section, we detail how we estimate our main empirical specification for the damage function on amenities and productivities and extend the damage functions to include temperature variability and sectoral heterogeneity.

B.1. *Estimation of Damage Functions*

In order to estimate the effect of temperature on amenities and productivities, we employ equation (3.21) as our main empirical specification. The variable $T_t(r)$ denotes the average temperature over the last decade for January in the Northern Hemisphere and July in the Southern Hemisphere, and $\mathbb{1}\{T_t(r) \in \mathcal{T}_j\}$ is an indicator function for temperature $T_t(r)$ being in the interval $\mathcal{T}_j$. We partition the distribution of temperature into $J = 20$ bins, each comprising 5% of the observed temperature values.

The variable $Z(r)$ is a vector of cell-level geographic attributes. Namely, mean, standard deviation and average deviation of elevation, distance to the coast, to a water body and to non-frozen oceans. Each of these six covariates, $Z_i(r)$, is transformed by means of a Chebyshev polynomial, $Z_i^j(r)$, $j \in \{1, \cdots, 5\}$. Accordingly, the vector $Z(r)$ comprises the 30 elements of $Z_i^j(r)$,

$$Z_i^j(r) = \cos\left(j \cdot \arccos\left(\frac{\tilde{Z}_i(r)}{\max_{s \in S} |\tilde{Z}_i(s)|}\right)\right), \quad \tilde{Z}_i(r) = Z_i(r) - \frac{1}{2}\left(\min_{s \in S} Z_i(s) + \max_{s \in S} Z_i(s)\right).$$

Additionally, we consider an indicator function for 16 different types of land.[8] With respect to the time-invariant fixed effects, $\iota(g)$, we partition the $180° \times 360°$ gridded map into blocks of size $2° \times 2°$. As for the time-varying fixed effects at the sub-national level, $\iota_t(s_x)$, we take as basis the sub-national levels, as delimited in Kummu et al. (2018), and aggregate the sub-national units in Europe at the (i) country-level, as defined in Desmet et al. (2018), and (ii) at the region level, considering North, South, West and East.[9,10]

8. $Z_i(r)$ denotes the variable in raw units (for instance, in meters when considering elevation) and $Z_i^j(r)$ the Chebyshev transformation for the j-th polynomial so that it lies between minus one and one.

9. We aggregate the sub-national units in Europe, because some of them have a size of one cell, precluding a proper identification.

10. Figure 82 in Supplementary Materials Section M.1 displays the spatial demarcations of the sub-national units.

We estimate equation (3.21), modeling the error term as in Conley (1999). That is, we consider that errors are spatially correlated, so that correlation linearly declines from one to zero as distance increases. When distance is greater than or equal to 550 km (5 cells) correlation is zero, as in Schlenker and Roberts (2009). We implement this error structure through the Stata package `acreg`, developed by Colella et al. (2019).

To smooth the behavior of the point estimates across temperature bins, $\hat{\delta}_j^x$, we fit the logistic curve $\delta^x(T)$, given by equation (B.2), across the point estimates of each bin, weighting them by the inverse of their standard errors, $\text{se}(\hat{\delta}_j^x)$, to provide a greater weight to the more accurate estimates. In other words, we estimate the coefficients $(\delta^x_{\text{min}}, \delta^x_{\text{max}}, \delta^x_{\text{center}})$ that solve[11]

$$\min \quad \sum_{j=1}^{J} \frac{1}{\text{se}(\hat{\delta}_j)} \left(\hat{\delta}_j - \delta^x(T_j)\right)^2 \tag{B.1}$$

$$\text{st} \qquad \delta^x(T) = \delta^x_{\text{min}} + \frac{\delta^x_{\text{max}} - \delta^x_{\text{min}}}{1+\text{e}^{0.1(T-\delta^x_{\text{center}})}}, \tag{B.2}$$

where T_j is the $(2j-1)/(2J)$-th percentile of the temperature observations, $j \in \{1, \cdots, J = 20\}$. To estimate the upper and lower $\alpha\%$ confidence interval of the logistic function, we solve (B.1), but replace the point estimates of each bin j by their upper and lower $\alpha\%$ confidence intervals, respectively.

B.2. *Temperature Variability*

The damage functions estimated in Section 3.2 capture the impact of changes in the average winter (January-July) temperatures on the fundamentals of the economy. However, higher concentrations of greenhouse gases might not only affect the first moment of the temperature distribution, but also second moments. Here, we extend the damage functions to incorporate different measures of temperature variability.

First, we collect gridded data on daily temperatures at a level of resolution of $1^\circ \times 1^\circ$ from the Berkeley Earth Surface Temperature. Then, we construct two measures of temperature variability at the cell-level: the standard deviation and the extreme temperature index. The standard deviation, $STD_t(r)$, measures the dispersion in daily temperature in period t and region r. The extreme temperature index, $ETI_t^c(r)$, is defined as the number of days per year in period t and region r with daily temperatures c degrees Celsius greater or lower than the local average, $\bar{T}_t(r)$, weighted by the size of the deviation. Namely,

$$ETI_t^c(r) = \sum_{d \in t} \frac{\left|T_{dt}(r) - \bar{T}_t(r)\right|}{\text{mean}_{d,r}\left|T_{dt}(r) - \bar{T}_t(r)\right|} \cdot \mathbb{1}\left\{\left|T_{dt}(r) - \bar{T}_t(r)\right| > c\right\},$$

where $T_{dt}(r)$ denotes the daily temperature on day d of period t. A one unit increase in $ETI_t^c(r)$ represents one additional day per year with average extreme temperature.

Figure 17 shows the spatial distribution of the two measures of temperature variability. For the extreme temperature index we use a threshold of 4°C, but the spatial pattern is preserved for other thresholds. Both variables show a similar spatial pattern:

11. To achieve convergence of the non linear estimation, we exogenously set to 0.1 the slope coefficient of the logistic function.

low dispersion in regions close to the Equator and higher dispersion in northern, or southern, latitudes. A comparison with Figure 4 reveals a strong negative correlation with January-July temperature.

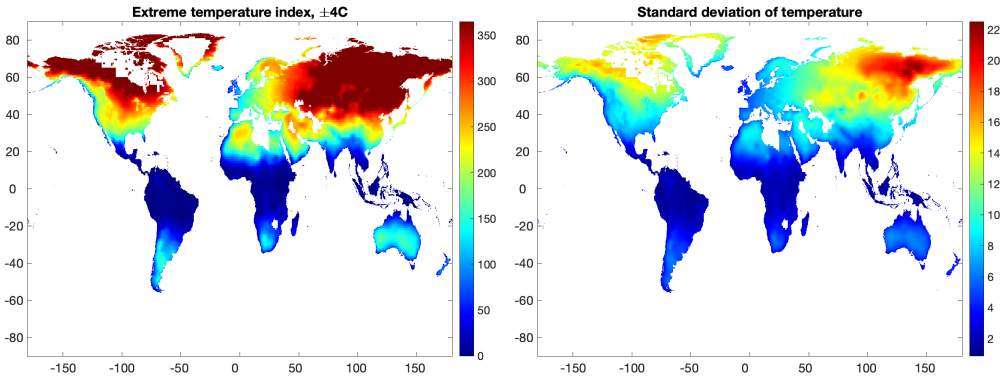

FIGURE 17

Extreme temperature index for the threshold 4°C and standard deviation of temperature.

We now extend our empirical specification of the damage functions using these measures of temperature dispersion. Namely, we estimate

$$\log(x_t(r)) = \sum_{j=1}^{J} \delta_j^x \cdot T_t(r) \cdot \mathbb{1}\{T_t(r) \in \mathcal{T}_j\} + \sum_{i=1}^{I} \mu_i^x \cdot M_t(r) \cdot \mathbb{1}\{T_t(r) \in \mathcal{T}_i\}$$
$$+ \delta^z \cdot Z(r) \cdot \mathbb{1}\{x_t(r) = \bar{a}_t(r)/\phi_t(r)\} + \iota(g) + \iota_t(s_x) + \varepsilon_t(r), \tag{B.3}$$

where, as before, $x_t(r) \in \{\bar{b}_t(r), \bar{a}_t(r)/\phi_t(r)\}$ are the fundamental amenities and the ratio of fundamental productivities to innovations at cell r in period t. The variable $T_t(r)$ denotes the January-July level of temperature and $M_t(r) \in \{ETI_t^c(r), STD_t(r)\}$ represents the temperature variability. Given the additive separable relation between these variables, the coefficient μ_i^x represents the semi-elasticity of $x_t(r)$ with respect to temperature variability.

We partition temperatures in $J = 20$ bins, as in the baseline, and $I = 5$ bins, to estimate the effect of temperature variability. We consider a small value of I to avoid bins with no variation in temperature dispersion, something that can happen in regions close to the Equator. Relative to our baseline specification for productivities that controls for geographic attributes, $Z(r)$, here we additionally control for fixed-effects at the 2×2 cell-level, $\iota(g)$. We include this covariate to control for any local characteristic that could affect the effect of variability on productivity. For amenities, we use only $\iota(g)$, as in the baseline. Supplementary Materials Section M.1 presents the estimates of μ^b and μ^a. In very cold regions, increases in temperature variability raise both amenities and productivities, because warmer days tend to have a larger impact than colder days. In bins with warmer temperatures, the beneficial effects of rising temperature variability decline. These results are robust to different measures of temperature variability. Of course, they represent only the partial effect of temperature variability on the fundamentals of the economy, after controlling for local January-July temperature, which explains why their level is always positive.

The extent to which temperature variability affects our baseline estimation of damage functions depends on the correlation between January-July temperatures and temperature variability after controlling for natural attributes. Namely, the R^2 of the regression $M_t(r) = \varkappa_0 + \varkappa \cdot T_t(r) + \varkappa^z \cdot Z(r) + \varepsilon_t(r)$. Table 4 shows the effect of a 1°C increase in January-July temperature on the variability measures, together with the R^2 of the regression. These two variables account for more than 92% of the variation for all our variability measures. Even more if we were to include block fixed-effects as well. This implies that the unexplained part of the variability measures cannot affect our damage functions significantly.

TABLE 4
Relationship between temperature variability and January-July temperatures.

	ETI^2	ETI^4	ETI^6	ETI^8	ETI^{10}	STD
$\varkappa$	−9.225***	−8.014***	−6.931***	−5.902***	−4.935***	−0.249***
	(0.103)	(0.0875)	(0.0812)	(0.0865)	(0.101)	(0.00292)
Observations	63.764	63.764	63.764	63.764	63.764	63.764
R^2	0.948	0.946	0.942	0.933	0.918	0.948

Spatially correlated standard errors in parentheses.
* $p<0.10$, ** $p<0.05$, *** $p<0.01$.

The semi-elasticities in our baseline estimation should therefore be closely related to $\delta_j + \mu_j \cdot \varkappa$ in the estimation with temperature variability. Figure 18 presents these semi-elasticities for the case of $c = 4$°C and, in gray, their logistic fit. For comparison, we also show the logistic fit of the baseline semi-elasticities. As expected, given the results in Table 4, they are very similar.[12] In sum, these results suggest that the baseline empirical specification captures not only the effects of changes in January-July temperatures, but also the effects of changes in temperature dispersion. The results for other measures of temperature variability are very similar.

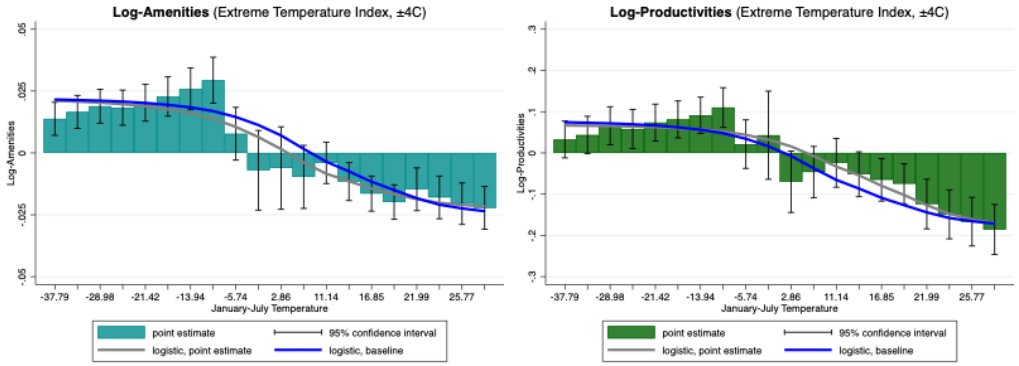

FIGURE 18
Aggregate effect of temperature on fundamental amenities and productivities, accounting for temperature variability.

12. The construction of the confidence intervals assumes that the coefficients of the augmented damage function and the one for the regression of variability on temperature are independent.

B.3. *Sectoral Composition*

Global warming can have heterogeneous effects across locations depending on their sectoral composition. Nath (2020) and Cruz (2021) both document a particularly large effect for agriculture. This could potentially bias our results since it implies that the semi-elasticities of temperature on fundamentals are a function of the sectoral composition. Hence, we extend our estimation of the damage functions to allow for this dependence, and simulate the model with the new damage functions to compare these results with those of the baseline scenario.

We focus on agriculture and the rest of the economy, given that this issue seems more salient for this classification, and data for agricultural production at a granular level is available from the Food and Agriculture Organization (FAO). We compute the share of value added in agriculture for each $1^\circ \times 1^\circ$ cell in the year 2000 as in Conte et al. (2021, 2022). Figure 19 shows that most locations of the world have a negligible contribution of agriculture to GDP. The regions with the highest intensities on agriculture are the North of Canada, Brazil, Sub Saharan Africa, North of China, Papua New Guinea, and Southwest Australia.

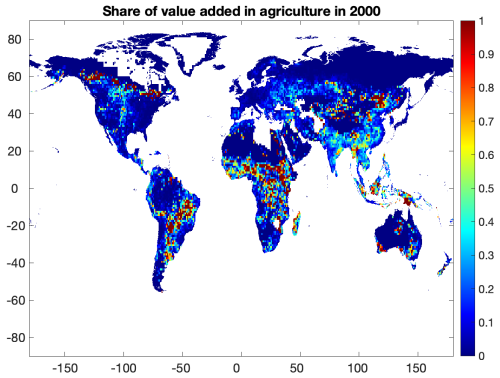

FIGURE 19
Share of value added in agriculture.

Then, we extend the damage function to integrate the interaction of temperature levels with the share of agriculture in value added, $s(r)$,

$$\log(x_t(r)) = \sum_{j=1}^{J} \delta_j^x \cdot T_t(r) \cdot \mathbb{1}\{T_t(r) \in \mathcal{T}_j\} + \sum_{i=1}^{I} \beta_i^x \cdot s(r) \cdot T_t(r) \cdot \mathbb{1}\{T_t(r) \in \mathcal{T}_i\}$$
$$+ \delta^z \cdot Z(r) \cdot \mathbb{1}\{x_t(r) = \bar{a}_t(r)/\phi_t(r)\} + \iota(g) \cdot \mathbb{1}\{x_t(r) = \bar{b}_t(r)\} + \iota_t(s_x) + \varepsilon_t(r). \tag{B.4}$$

We partition the distribution of temperatures into $J = 20$ and $I = 5$. We set $I < J$ to avoid bins with no variation in the share of agriculture, something prevalent in regions with negligible shares of agriculture. The semi-elasticity of $x_t(r)$ with respect to temperature, $\delta_j^x + \beta_i^x \cdot s(r)$, is now allowed to vary according to the level of temperature and the share of agriculture in value added.[13]

13. We could additionally control for the share of agriculture in equation (B.4), but it is already captured by the natural attributes, $Z(r)$, and the block fixed effects, $\iota(g)$.

Figure 20 presents the results of the estimation. The colored bars show the point estimates for cells where no agriculture is performed, $s(r)=0$, and the gray bars those for cells that exclusively produce agricultural goods, $s(r)=1$. Our empirical results imply that agriculture is more climate-sensitive than the rest of the economic sectors for both cold and hot regions and both amenities and productivities. In the coldest locations of the world, an increase in local temperature of 1°C generates a productivity improvement about twice as large when a location is fully devoted to agricultural activities. We observe a negative effect of similar magnitude when temperature rises in the hottest locations of the world. For amenities, there is a similar relationship, although the costs at warm temperatures seem to depend less on the agricultural share.

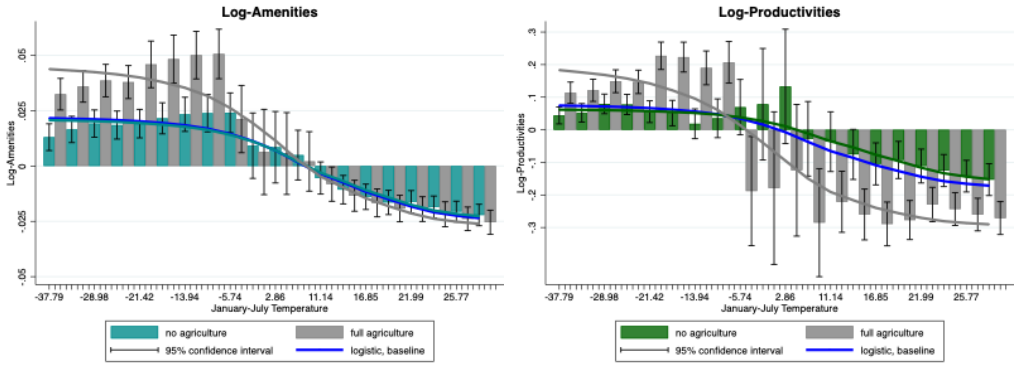

FIGURE 20
Aggregate effect of temperature on fundamentals, accounting for differences in the share of agriculture in value added.

Figure 20 also plots the logistic smoothing for the baseline estimation. Since the global share of agriculture is low, the logistic smoothing for no agriculture closely approximates that of the baseline estimation. To simulate the model accounting for the role of agriculture in shaping the damage functions, we construct eleven curves, given by the logistic smoothing of $\delta_j^x+\beta_i^x\cdot s$, with $s\in\{0,0.1,\cdots,1\}$, and allocate the damage function that best approximates the agricultural share of each cell in year 2000. We simulate the model under the assumption that the share of agriculture remains constant over time. Figure 21 shows a similar spatial pattern of welfare losses relative to that of Figure 8. The discrepancies, evident from the more pronounced colors, correspond to the zones largely devoted to agricultural activities. Since most of these locations lie in the coldest zones of the world, global welfare and real GDP losses are now 1 and 0.7 percentage points lower, respectively. Over time, we observe an attenuation of warming impacts. Figure 22 shows that during the current century, the differences are negligible. Nevertheless, by the end of the simulation, welfare and real GDP losses decline by roughly two percentage points when we incorporate agricultural shares. Of course, in a couple of centuries, agricultural shares might be very low everywhere as more countries go through a structural transformation.

C. NATALITY RATES, ENERGY ELASTICITIES AND MIGRATION COSTS

In this subsection, we outline the procedure to estimate the parameters of the natality rate function, b^ℓ,b^h,b^T, b^w, the elasticities of energy productivity growth to global real

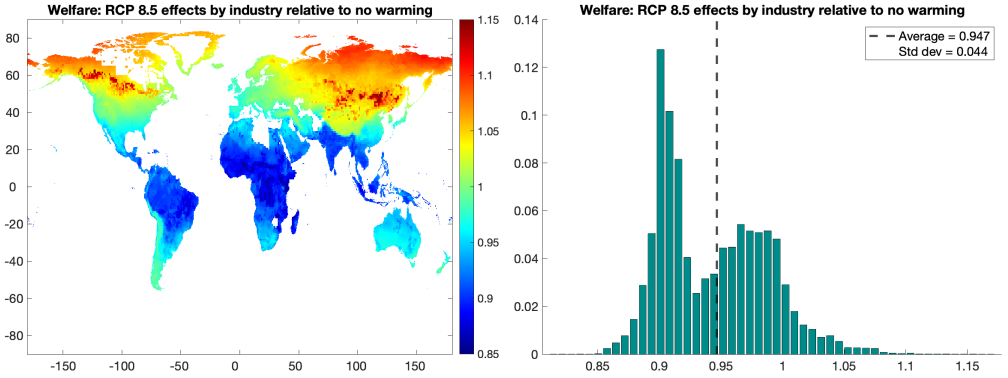

FIGURE 21
Welfare losses due to global warming with differences in the share of agriculture in value added.

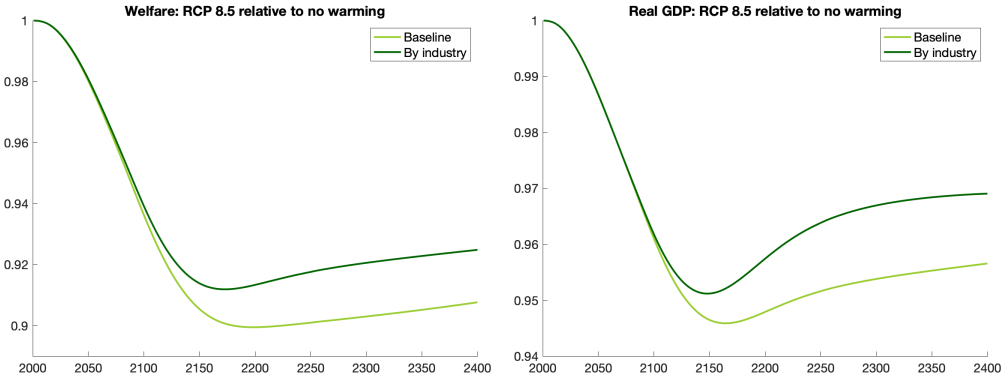

FIGURE 22
Welfare and real GPD under baseline and with differences in the share of agriculture in value added.

GDP growth, υ^f, υ^c and the migration cost function, $m_2(\cdot)$. To construct the natality rate function $\eta(\cdot)$, we set the parameter b_0^T to target the global natality rate observed in the year 2000, n_0^w, and we impose the functional form of equation (3.23),

$$
\begin{aligned}
&n_0^w L_0 - \int_S \eta^y(\log(y_0(v)); b^\ell, b^h) L_0(v) H(v) \mathrm{d}v = \\
&\int_S \eta^T(T_0(v), \log(y_0^w); b^T, b_w) L_0(v) H(v) \mathrm{d}v = \\
&(0.5) b_0^T L_0 + (0.5) b_2^T \int_S \left(\mathrm{e}^{-b_1^T (T_0(v) - b^{*T})^2} \right) L_0(v) H(v) \mathrm{d}v.
\end{aligned}
$$

Hence, we can define b_0^T as a function of the remaining parameters $\flat = (b^\ell, b^h, b_1^T, b_2^T, b^{*T})$ and data on the initial period $x_0 = (n_0^w, L_0(\cdot), y_0(\cdot), T_0(\cdot))$. Local population is obtained from the G-Econ database, local real income is constructed as $y_0(r) = L_0(r)^\lambda u_0(r) / \bar{b}_0(r)$ so that the ratio of utility to amenities is computed as in

Supplementary Materials Section I.2,[14] and local temperature comes from the Berkeley Earth Surface Temperature Database (BEST, Rohde and Hausfather, 2020),

$$b_0^T(\flat,x_0)=2n_0^w-\frac{1}{L_0}\int_S\left(2\eta^y(\log(y_0(v));b^\ell,b^h)+b_2^T\mathrm{e}^{-b_1^T\left(T_0(v)-b^{*T}\right)^2}\right)L_0(v)H(v)\mathrm{d}v. \tag{C.5}$$

Analogously, we set the parameter b_w to target the global natality rate observed in the year 2020, n_{20}^w. The natality rates n_0^w and n_{20}^w are taken from the World Population Prospects of the United Nations,

$$\begin{aligned}&n_{20}^wL_{20}-\int_S\eta^y(\log(y_{20}(v));b^\ell,b^h)L_{20}(v)H(v)\mathrm{d}v=\\&\int_S\eta^T(T_{20}(v),\log(y_{20}^w);b^T,b_w)L_{20}(v)H(v)\mathrm{d}v=\\&\frac{1}{1+\mathrm{e}^{b_w[\log(y_{20}^w/y_0^w)]}}\int_S\left(b_0^T(\flat,x_0)+b_2^T\mathrm{e}^{-b_1^T\left(T_{20}(v)-b^{*T}\right)^2}\right)L_{20}(v)H(v)\mathrm{d}v.\end{aligned} \tag{C.6}$$

Hence, we can define b_w as a function of the parameters $\flat$ and data on the initial and twentieth period,

$$b_w(\flat,x_0,x_{20})=\frac{1}{\log(y_{20}^w/y_0^w)}\log\left(\frac{\int_S\left(b_0^T(\flat,x_0)+b_2^T\mathrm{e}^{-b_1^T\left(T_{20}(v)-b^{*T}\right)^2}\right)L_{20}(v)H(v)\mathrm{d}v}{n_{20}^wL_{20}-\int_S\eta^y(\log(y_{20}(v));b^\ell,b^h)L_{20}(v)H(v)\mathrm{d}v}-1\right). \tag{C.7}$$

Now, we describe the algorithm employed to jointly solve for the parameters and functions of interest.

1. Guess $m_2(\cdot),\flat,\upsilon^f,\upsilon^c$ and x_{20}.
2. Run the model backwards for 50 periods using equation (I.50) of Supplementary Materials Section I.4, taking the behavior of local historical temperature as in the BEST data,[15] and retrieve $L_t(\cdot)$ and $y_t(\cdot)$.
3. Compute the natality rates at the country-level induced from the model.[16] If the difference between the model induced and the historical natality rates is small enough, go to the next step. Otherwise, use the solution of (C.8) to update $\flat$ and go back to step 2,

$$\min_{\flat}\quad SSR(\flat)=\sum_{c=1}^{168}\sum_{t=1950}^{1999}L_t^c\left(n_t^{c,data}-n_t^{c,model}(\flat)\right)^2 \tag{C.8}$$

14. To solve for this ratio we require data on local wages and energy prices, which come from G-Econ, EDGAR and BP databases. Further details of the data are described in Online Appendix A.

15. The backward solution of the climatic model does not provide very accurate results with respect to the historical observations. Therefore, we prefer to employ observed past data.

16. We consider 168 countries, following the classification of Desmet et al. (2018).

$$\text{st} \qquad n_t^{c,model}(\flat) = \frac{\int_{v\in c}\eta(\log(y_0(v)),T_t(v);\flat)L_t(v)H(v)\mathrm{d}v}{\int_{v\in c}L_t(v)H(v)\mathrm{d}v},$$

where c denotes countries, t periods of time, L_t^c the weight given to each observation, based on historical country-level population data, and u_t^c the error between the model and the data for each observation.

We solve (C.8) as follows: If $SSR(\cdot)$, evaluated at the guess, is small enough, the procedure ends. Otherwise, we update $\flat$ in the j-th iteration as $\flat_{j+1} = \flat_j + \varrho(X_j'DX_j)^{-1}(X_j'Du_j)$, where X_j is a matrix of size $(168\cdot 50)\times B$ comprising the derivatives of $n_t^{c,model}(\cdot)$ evaluated at $\flat_j$, D a matrix of size $(168\cdot 50)\times(168\cdot 50)$ comprising the population weights, u_j a matrix of size $B\times(168\cdot 50)$ comprising the errors evaluated at $\flat_j$, and B the number of elements in the vector $\flat$.

At each iteration, the *step size* scalar parameter ϱ is set to one, and a candidate $\flat_{j+1}^*$ is computed from the above procedure. If $SSR(\flat_{j+1}^*) < SSR(\flat_j)$, then $\flat_{j+1} = \flat_{j+1}^*$ and the iteration is completed. Otherwise, ϱ is halved, a new $\flat_{j+1}^*$ is computed, and the process is repeated. The non-linear least square estimation concludes when $SSR(\flat_{j+1})$ is small enough.

4. Compute the migration costs that target population distribution in the year 2005 using equation (I.54) of Supplementary Materials Section I.5. If the difference between the guess and the targeted migration costs is small enough, run the model 20 periods in the future, update x_{20} and go to the next step. Otherwise, use the targeted migration costs to update $m_2(\cdot)$ and go back to step 2.[17]
5. If the difference between the model induced, $E_t^{f,model}$, and historical data on global emissions, $E_t^{f,data}$, from 1950 to 1999 is small enough, run the model 20 periods in the future, update x_{20} and go to the next step. Otherwise, update $\upsilon^f = (E_{1999}^{f,data} - E_{1950}^{f,data})/(E_{1999}^{f,model} - E_{1950}^{f,model})$ and go back to step 2.
6. If the difference between the model induced, $E_t^{c,model}$, and historical data on global clean energy use, $E_t^{c,data}$, from 1965 to 1999 is small enough, run the model 20 periods in the future, update x_{20} and the algorithm concludes.[18] Otherwise, update $\upsilon^c = (E_{1999}^{c,data} - E_{1965}^{c,data})/(E_{1999}^{c,model} - E_{1965}^{c,model})$ and go back to step 2. The goodness of the fit for CO_2 emissions, clean energy use, and natality rates is presented in Supplementary Materials Section K.

D. CARBON CYCLE AND TEMPERATURE DOWN-SCALING

In this section, we describe the parametrization of the carbon cycle and the temperature down-scaling. Regarding the evolution of the stock of carbon dioxide, displayed in equation (2.13), the share of CO_2 remaining in the atmosphere ℓ periods ahead, $(1-\delta_\ell) = a_0 + \sum_{i=1}^{3}(a_i \cdot \mathrm{e}^{-\ell/b_i})$, is approximated by a sum of exponentials, as in Forster et al. (2007) and Joos et al. (2013). According to IPCC (2013), we set $a_0 = 0.2173, a_1 = 0.2240, a_2 = 0.2824, a_3 = 0.2763, b_1 = 394.4, b_2 = 36.54, b_3 = 4.304$. To simplify the evolution

17. Figure 54 in Supplementary Materials Section K displays the logarithm of migration costs of the last iteration of the algorithm.

18. The BP database does not contain information on clean energy use for the years 1950-1964.

of carbon stock, we rewrite the law of motion as

$$S_{t+1} = S_{0,t+1} + \sum_{i=1}^{3} S_{i,t+1}, \quad S_{0,t+1} = S_{0,t} + a_0(E_t^f + E_t^x), \tag{D.9}$$

$$S_{i,t+1} = (\mathrm{e}^{-1/b_i})S_{i,t} + a_i(E_t^f + E_t^x), \quad i \in \{1,2,3\}. \tag{D.10}$$

Thus, the model requires the initial values of the four layers, $S_{0,i}, i \in \{0,1,2,3\}$. Following Golosov et al. (2014), we consider $S_{0,2000} = 2{,}429$ $\mathrm{GtCO_2}$ as the sum of the pre-industrial stock, $S_{\text{pre-ind}} = 2{,}200$ $\mathrm{GtCO_2}$, plus a share a_0 of the historical cumulative carbon emissions, $\sum_{\ell=1945}^{1999}(E_\ell^f + E_\ell^x) = 1{,}054$ $\mathrm{GtCO_2}$. The remaining three layers, $S_{1,2000} = 224, S_{2,2000} = 178, S_{3,2000} = 37$ $\mathrm{GtCO_2}$, are computed as the discounted sum of past emissions.[19]

The response of global temperature to a unit of forcing can be represented by a sum of two exponentials, $\zeta_\ell = \sum_{j=1}^{2}(c_j/d_j)\cdot \mathrm{e}^{-\ell/d_j}$, as in Boucher and Reddy (2008). We take the forcing sensitivity to be $\varphi = 5.35$ and the climate parameters to be $c_1 = 0.631, c_2 = 0.429, d_1 = 8.4, d_2 = 409.5$.[20] Analogously to the carbon circulation, we rewrite the global temperature module as

$$T_{t+1} = T_{1,t+1} + T_{2,t+1}, \quad T_{j,t+1} = (\mathrm{e}^{-1/d_j})T_{j,t} + \frac{c_j}{d_j}F_{t+1}, \quad j \in \{1,2\}, \tag{D.11}$$

where $T_{1,2000} = 1.01°\mathrm{C}$ is the discounted sum of past forcings (from 1825 to 2000) and $T_{2,2000} = 8.19°\mathrm{C}$ is the discounted sum of past forcings plus the pre-industrial temperature $T_{\text{pre-ind}} = 8.1°\mathrm{C}$. We interpret temperature as that over land, excluding that over water.

To construct the mapping from global to local temperature, we estimate equation (2.16), where the object of interest is the temperature scaler function, $g(\cdot)$. We parametrize this function as an additive separable Chebyshev polynomial of order 10 in the following arguments: latitude, longitude, product of latitude and longitude, mean elevation, distance to the coast, distance to the ocean, distance to a water body, vegetation density, albedo and share of land covered by ice. Therefore, we can define the function $g(\cdot)$ as shown in equation (D.12), where $X_i(\cdot)$ denotes each of the ten covarites mentioned in the previous paragraph, $X_i^j(\cdot)$ is the Chebyshev polynomial of order $j \in \{1,\cdots,10\}$ of covariate i and β_i^j is the set of coefficients to be estimated by

19. Historical data for $\mathrm{CO_2}$ stock and projections for $\mathrm{CO_2}$ emissions and forcing for every RCP are taken from http://www.iiasa.ac.at/web-apps/tnt/RcpDb.

20. Etminan et al. (2016) provides new calculations of the radiative force with respect to Myhre et al. (1998). They propose a GHG concentration-dependence for the forcing sensitivity, so that it can be expressed as $\varphi = 5.35 + \varphi_1|S_t - S_{\text{pre-ind}}| + \varphi_2(S_t - S_{\text{pre-ind}})^2 + \varphi_N(N_t + N_{\text{pre-ind}})/2$, where N_t denotes the stock of nitrous oxide.

OLS,[21]

$$g(r)=\sum_{i=1}^{10}\sum_{j=1}^{10}\beta_i^j X_i^j(r), \quad X_i^j(r)=\cos\left(j\cdot\arccos\left(\frac{\tilde{X}_i(r)}{\max_{s\in S}|\tilde{X}_i(s)|}\right)\right), \tag{D.12}$$

$$\tilde{X}_i(r)=X_i(r)-\frac{1}{2}\left(\min_{s\in S}X_i(s)+\max_{s\in S}X_i(s)\right).$$

To estimate (2.16) and (D.12), we construct the temperature variables as follows: $T_{\text{base}}(r)$ is the average January-July temperature from 1950 to 1979 in cell r, $T_t(r)$ is the yearly January-July temperature from 1980 to 2017 in cell r, and T_{base} is the global average temperature, where each cell is weighted by land size. Finally, we provide more weight to more recent observations, according to $\omega_t=(2018-t)^{-1}$. The estimation procedure is able to capture 83% of variation in the data.

E. ADDITIONAL RESULTS FOR THE BASELINE RCP 6.0 QUANTIFICATION

Figure 23 shows the ratio of fundamental amenities and productivities in 2200 in the baseline scenario relative to the counterfactual scenario without global warming, Figure 24 presents the evolution of global population and population density in 2200 in the baseline scenario relative to the counterfactual scenario without global warming and Figure 25 displays the uncertainty in welfare losses from damage functions and elasticity of substitution between energy sources, all of them for the RCP 6.0 quantification.

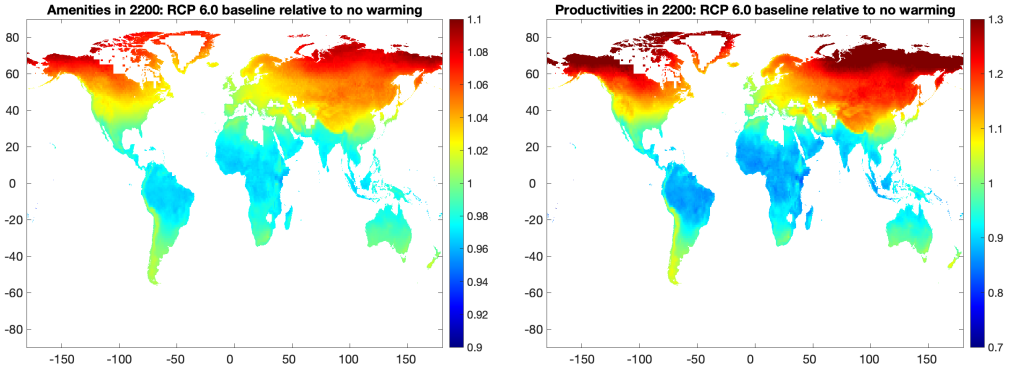

FIGURE 23
Gains and losses in amenities and productivities from global warming RCP 6.0 in the year 2200.

F. DECOMPOSING THE LOSSES FROM GLOBAL WARMING BY SOURCE

As we argued in the main text, the two main direct channels through which global warming affects economic outcomes are the effects on amenities and productivities.

21. When constructing the product of latitude and longitude, we first normalize latitude and longitude so that they lie between minus one and one, and then we multiply them. That is, we define this product as $X_{\text{lat}}^j(\cdot)\times X_{\text{lon}}^j(\cdot)$.

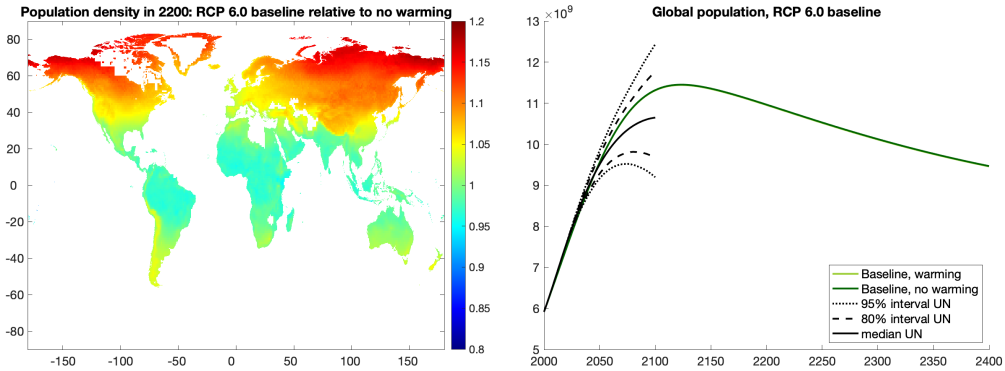

FIGURE 24
Spatial pattern of population and global population, RCP 6.0.

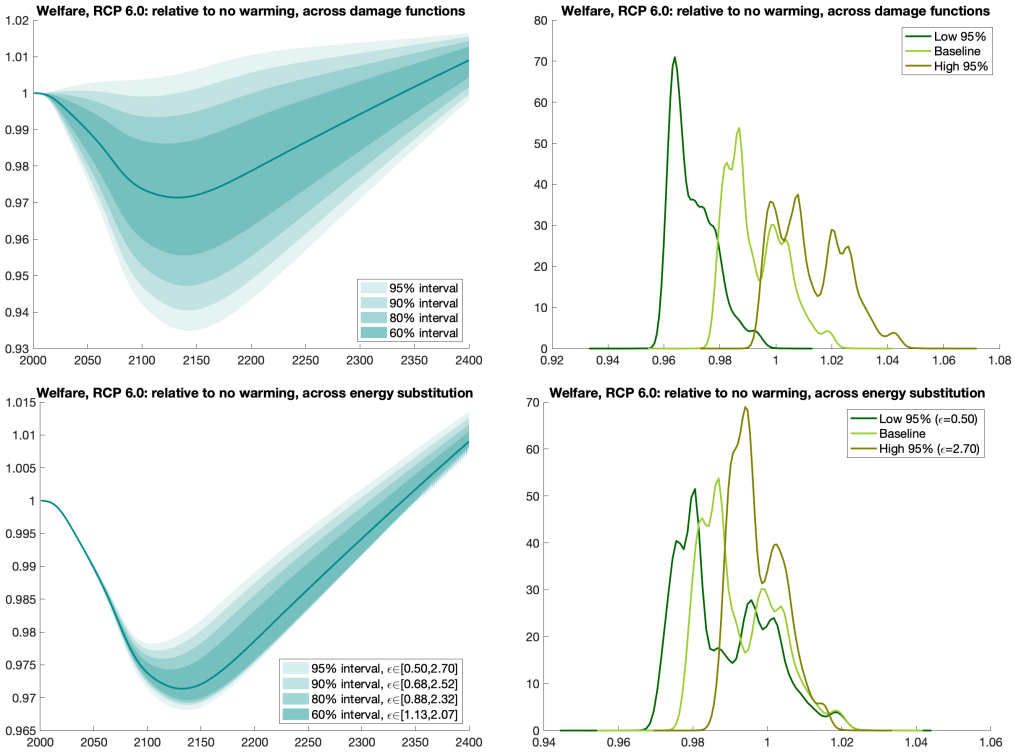

FIGURE 25
Uncertainty in welfare losses from damage functions and energy substitution, RCP 6.0.

In fact, incorporating the effect of temperature on amenities at this level of spatial disaggregation is, we believe, novel to our study. To understand the contribution of each of these two sources of economic effects, we decompose the warming damages as those arising exclusively from the effect of temperature on local amenities and those arising exclusively from the effect of temperature on local productivities. That is, we calculate

two additional counterfactual scenarios setting each of the damage functions to zero for every period and cell, respectively.

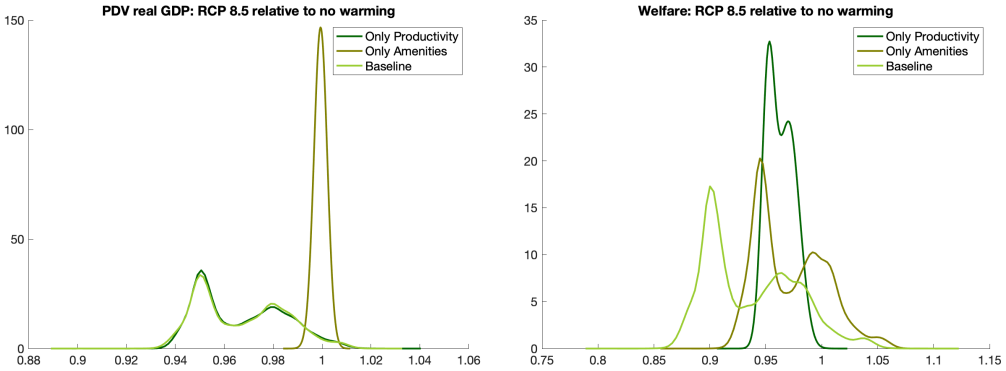

FIGURE 26
Distribution of real GDP and welfare losses by damage source.

Figure 26 compares the cross-section of losses in the PDV of real GDP and welfare across damage sources. The spatial distribution of real GDP losses is mainly driven by the productivity component. The amenity component affects real GDP through its effect on the spatial distribution of population and the corresponding effects of investment. However, the effects are small compared to the direct impact of productivity. In contrast, when we analyze the cross-sectional distribution of welfare, the role of amenities is very large and governs the overall shape of the distribution. For welfare, the productivity component is more uniform across regions with implied losses for almost all locations. This exercise highlights the importance of incorporating the effect of changes in temperature on amenities when assessing the local welfare impact of global warming.

Figure 27 displays the spatial composition of losses in welfare when the damage function only takes into account damages on amenities or productivities, respectively. The large dispersion in the effect coming exclusively from amenities implies large gains in Russia, Canada, and Alaska, and losses in South America, Africa, and India. In contrast, the spatial distribution of the effects coming exclusively through the productivity channel implies losses in most of the southern regions. All southern regions, including Australia, suffer, and the losses reach further north to Mexico and the Southern part of the U.S., as well as India and China. Clearly, the spatial distribution of the losses from global warming that result from each source are quite different.

To end this section, Figure 28 decomposes the evolution of economic losses over time. When we consider damages on amenities only, cold regions become more amenable for living, which creates an incentive for people to move to some of the most productive places in the world. This migration boosts agglomeration and thus raises global average real GDP slightly for the first 200 years. Eventually, as temperatures decline due to the rising cost of extracting fossil fuels, this process reverses. Welfare, in contrast, exhibits only losses that accelerate as rising temperatures deteriorate amenities in the developing world. When we isolate the damages from warming coming from changes in local fundamental productivity, the evolution of losses in real GDP is similar to the baseline scenario for the first century. Without the impact of climate on amenities, however, less people move north which results in less agglomeration and slightly larger real GDP losses. The difference is much larger when considering welfare. The effect

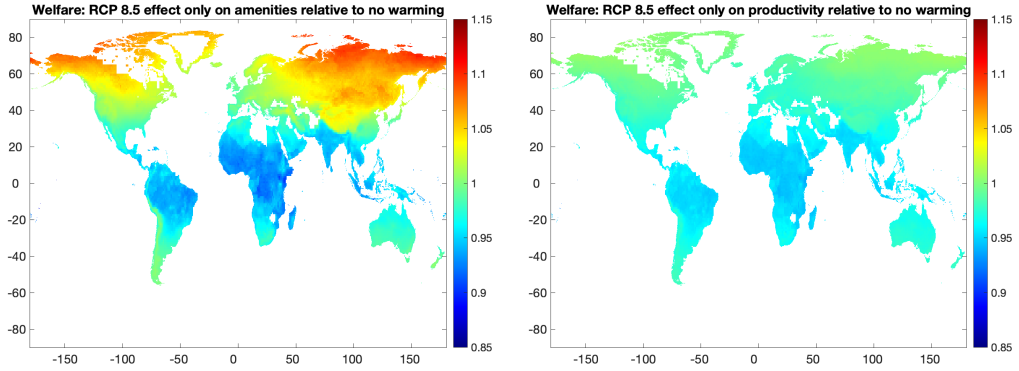

FIGURE 27
Spatial distribution of real GDP and welfare losses due to global warming by damage source.

on amenities essentially doubles the impact of global warming on welfare throughout. Overall, Figure 28 shows that the effect of temperature on fundamental productivity and the effect of temperature on amenities, each account for about half of the total welfare losses from global warming.

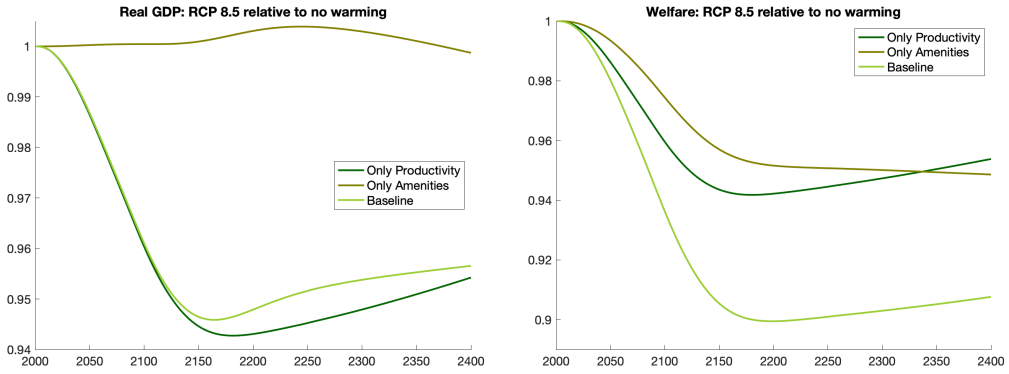

FIGURE 28
Real GDP and welfare losses by damage source over time.

G. ADDITIONAL ADAPTATION RESULTS

G.1. *Dispersion of Idiosyncratic Preferences*

As an alternative way to measure the importance of migration as an adaptation mechanism, we modify the variance of the idiosyncratic shocks governing taste across locations. A greater value of Ω implies more dispersion in agent's preferences across regions, so that mobility responses are mostly driven by idiosyncratic motives, rather than spatial differences in utility adjusted for the migration cost of entering the region. Consequently, the parameter $1/\Omega$ can be interpreted as the elasticity of migration to $u_t(r)/m_2(r)$, as shown in equation (2.2). A higher $1/\Omega$ therefore implies a larger elasticity of migration to the factors driving utility, $u_t(r)$, which, as in standard spatial models, leads to more migration. However, it also implies a larger elasticity to the frictions to

enter a region, $m_2(r)$, which results in smaller migration to regions that are hard to enter. The implications for overall migration are, therefore, not straightforward and depend on the direction of flows and the geography of $m_2(r)$. Below, we evaluate the spatial and temporal impacts of global warming to reductions in the parameter Ω to 50% and 25% of its baseline value.

Figure 29 displays the effects of climate change on welfare, when considering economies with lower Ω. The left panel presents the difference-in-difference effect of Ω on the effect of temperature. Red areas experience larger losses (or smaller gains) with larger $1/\Omega$, while the opposite is the case for blue areas. A larger $1/\Omega$ has a negative effects on northern and southern regions, as they become less populated, inhibiting innovation. For these areas, the effect of $1/\Omega$ acts as a detriment to migration. Consistently, regions close to the Equator, which are easy to enter, benefit from preserving population in those locations (since they now feature less congestion due to the higher migration elasticity to $u_t(r)$). By reducing mobility across space, a higher elasticity $1/\Omega$ deepens the aggregate welfare losses over time: diminishing the parameter Ω to a quarter of its original value rises global welfare losses by 2 percentage points (see right panel of Figure 29).

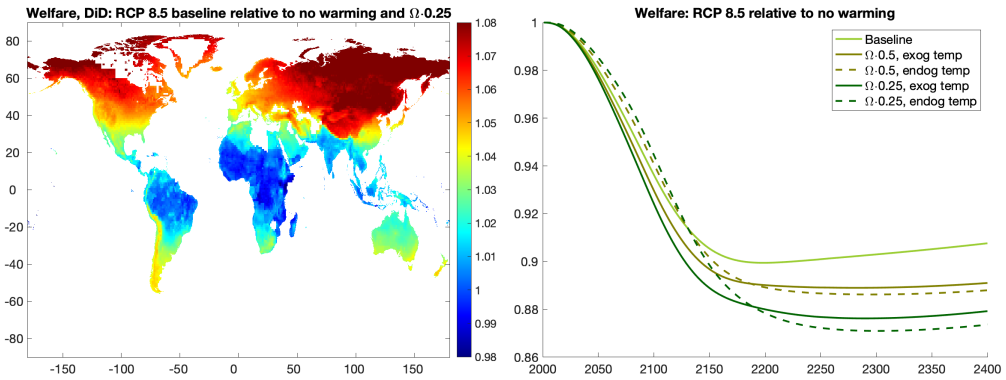

FIGURE 29
Welfare across different migration elasticities.

G.2. *Imposing Border Frictions*

In this subsection, we describe our methodology to compute migration costs within and across a border. We also present an additional evaluation of the impacts of global warming when rising the costs of migrating from the developing into the developed world. First, we extend the specification of the migration costs, while preserving their multiplicative structure,

$$m(r,r') = \begin{cases} 1 & \text{if } r = r', \\ m_1(r) m_2(r') & \text{if } r \neq r', \mathcal{D}(r) = \mathcal{D}(r'), \\ m_1(r) n_1(\mathcal{D}(r)) m_2(r') n_2(\mathcal{D}(r')) & \text{if } r \neq r', \mathcal{D}(r) \neq \mathcal{D}(r'), \end{cases}$$

where $\mathcal{D}(\cdot)$ is a function mapping each cell to a region (e.g., Africa and Rest of the World, or developing and developed world). Staying in the same cell entails no cost. Moving within each region involves a cost given by the product of an origin-, $m_1(r)$, and a destination-specific cost, $m_2(r')$. Moving across regions implies a cost

given by the product of an origin-, $m_1(r)\cdot n_1(\mathcal{D}(r))$, and a destination-specific cost, $m_2(r')\cdot n_2(\mathcal{D}(r'))$. Since staying in the same location is costless, $m_1(r)=1/m_2(r)$ and $n_1(\mathcal{D}(r))=1/n_2(\mathcal{D}(r))$. Note that when setting $n_2(\mathcal{D}(r))=1$ for each r, we go back to our baseline specification.

Second, we construct the functions $m_2(\cdot)$ and $n_2(\cdot)$ as follows. We use the procedure outlined in Supplementary Materials Section I.5 to construct the migration costs, and we name the resulting estimate $\tilde{m}_2(\cdot)$. Then, we define the function $n_2(\cdot)$ as the weighted average of $\tilde{m}_2(\cdot)$, with weights given by the population shares of the year 2000,

$$n_2(d)=\left(\int_S \tilde{m}_2(r)L_0(r)H(r)\cdot\mathbb{1}\{\mathcal{D}(r)=d\}\,\mathrm{d}r\right)\left(\int_S L_0(r)H(r)\cdot\mathbb{1}\{\mathcal{D}(r)=d\}\,\mathrm{d}r\right)^{-1}.$$

We define the function $m_2(\cdot)$ as, $m_2(r)=\tilde{m}_2(r)/n_2(\mathcal{D}(r))$. Consequently, $m_2(\cdot)$ governs the cost of moving within a region and $n_2(\cdot)$ the cost of moving across regions.

Doubling the Cost of Migrating to the Developed World. Figure 30 presents the welfare impact of climate change in the baseline relative to the case where we double the cost of entering the developed world (the regions included as part of the developing world are outlined in black in the figure). As before, red areas have larger losses when the border frictions are more stringent. The left panel shows that the most affected regions are northern latitudes, due to the reduction in in-migration and, hence, innovation. The South of the United States, Western Europe, and Australia display lower welfare losses from global warming with higher border costs. In the baseline scenario, those places experience null or small negative impacts from global warming. Now, they benefit from the larger demand for their residents in northern locations, induced by climate change. The lower congestion costs also help them. The right panel shows that higher welfare costs of moving from the developing to the developed world affects both regions negatively. Importantly, a one hundred percent rise in the border costs implies that welfare losses increase by 2.5 times in the developed world over the long-run.

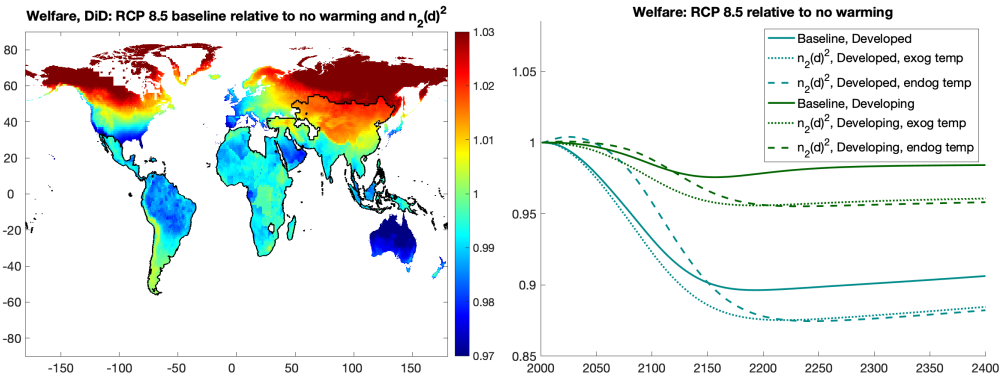

FIGURE 30
Welfare with higher costs of moving from the developing to the developed world.

G.3. *Trade*

Figure 31 presents the spatial and dynamic effect on welfare when rising trade costs to 1.5 and 2. The left panel presents the spatial distribution of the relative effect of global

warming on welfare in the baseline scenario with respect to the same relative effect in the scenario with higher trade costs. In this difference-in-differences calculation, large values, represented in red, identify areas that are hurt by larger trade costs. As is evident in Figure 31 trade costs have a negligible effect on the cost of global warming.

The spatial pattern in Figure 31 is markedly different than the one for migration. As with migration, larger trade costs make warming more harmful in Africa, India, and China. However, it also makes warming more harmful in Central and South America, as well as Europe, and less harmful in northern regions in Canada, Scandinavia, and Russia. Trade has little impact on northern regions since their relative isolation implies that they trade little with the rest of the world anyway. In contrast, regions in more central, well connected geographies, rely more on trade and so they suffer from the double impact of higher trade costs and higher temperatures. In addition, as with migration, higher trade costs reduce incomes which results in higher natality rates, particularly in the developed world, leading to additional congestion. Brazil, Africa, and India are affected the most.

The right panel of Figure 31 shows the temporal evolution of average welfare. The small effect of trade is evident, particularly when conditioning on the temperature path (solid curves). Once we take the effect of changes in income and population on the evolution of temperature into account (dashed curves), we get smaller losses from global warming with higher trade costs in the short-run, but larger ones in the long-run. Overall, adaptation through trade seems to play only a minor role in our results.

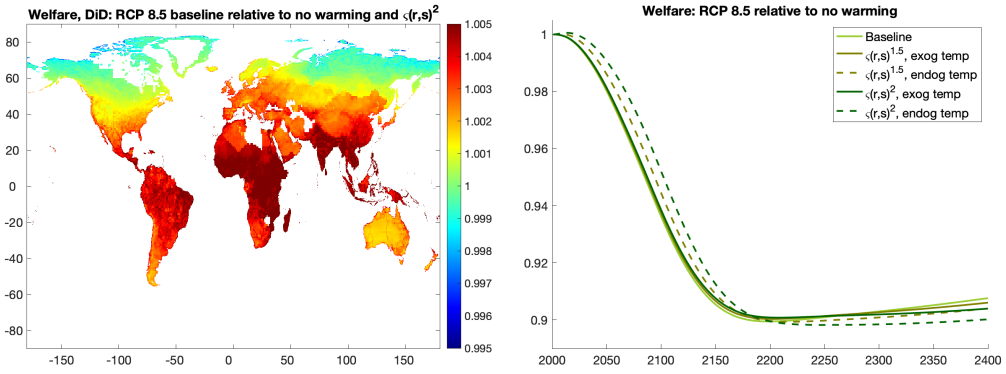

FIGURE 31
Welfare across different iceberg trade costs.

G.4. *Innovation*

Firm investments respond to market size and allow a region's technology to grow relative to that of other regions. Innovation improves northern regions' productivity, as they become warmer and gain population. It also accelerates the relative losses of regions that get too warm and lose market size due to the implied lower productivity and lower amenities. We study here the effect of lowering γ_1 (or, equivalently, increasing ξ). Changes in these parameters amount to changing the returns or cost of innovation proportionally across locations. Larger costs of innovation reduce real GDP growth and, therefore, growth in CO_2 emissions, curbing the temperature path. As with trade and migration costs, the lower real GDP growth pushes upwards natality rates and global population.

Figure 32 presents the spatial and dynamic implications of lower innovation returns (or higher innovation costs). The left panel presents the difference-in-differences for the

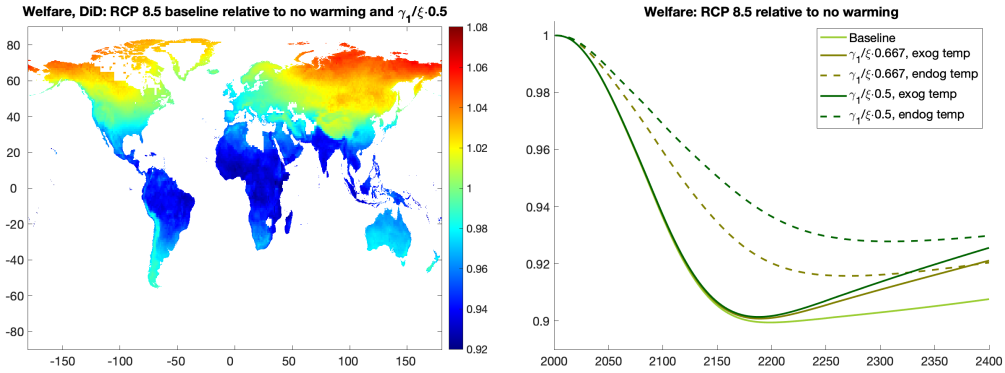

FIGURE 32
Welfare across different innovation costs.

welfare consequences of global warming in the baseline relative to the exercise with high innovation costs. The spatial pattern of this measure is simpler than the one for migration. The upmost northern regions are hurt more (benefited less) by global warming when innovation costs are higher. Developing these areas by improving their productivity and moving economic activity to the north becomes more costly. The same phenomenon is apparent in the upmost southern regions, including Oceania and the southern tip of South America and Africa.

The right panel of Figure 32 presents the dynamic evolution of the cost of global warming. In all cases, with and without feedback effects from temperature, larger innovation costs lead to smaller losses from global warming.[22] The reason is that larger innovation costs imply smaller benefits from density in locations that are eventually negatively affected by higher temperatures. In particular, Africa, India, and China experience lower technology growth and, therefore, attract less migrants from other locations. Given that these are the regions more affected by temperature rises, the average cost from this phenomenon declines. This effect builds up over time and is significant only after 2150. These results illustrate the importance of studying the impact of adaptation mechanisms in a spatial model. The reason that higher innovation costs result in smaller costs from global warming is fundamentally spatial, as explained above.

H. ADDITIONAL RESULTS ON ENVIRONMENTAL POLICIES

H.1. *Effect of Carbon Taxes Across Space*

Figure 33 displays the welfare impact across locations of a spatially and temporally constant carbon tax of 200%.

22. This result is robust to different values of the elasticity of utility to real income. As argued in Supplementary Materials Section L.4, lower values of this parameter modify the level of utility, but not allocations. Since the effect of innovation costs on welfare losses depends on the spatial distribution of economic activity, higher innovation costs reduce welfare losses, albeit by different amounts, according to the elasticity of utility to real income.

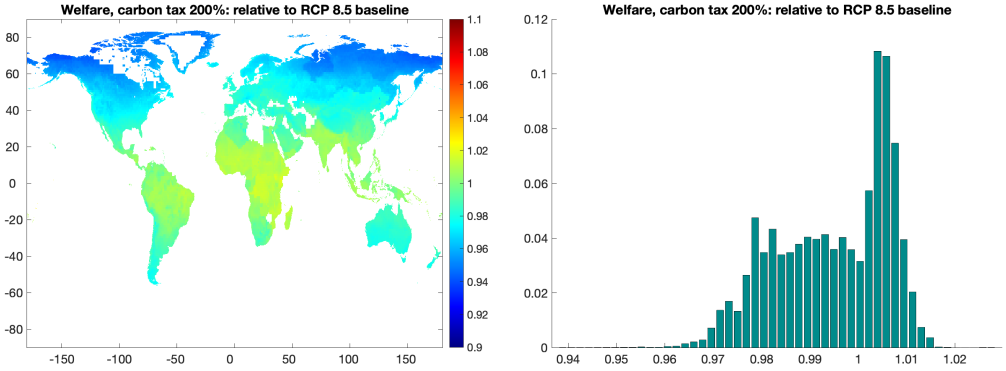

FIGURE 33

Local welfare effects of a carbon tax of 200% with a discount factor of $\beta = 0.965$.

H.2. *Abatement*

Here, we present the evolution of CO_2 emissions, temperature, real GDP and welfare over time with carbon taxes and an abatement technology that appears in 2100. Figure 34 introduces the abatement technology to the exercises presented in Figure 13. The solid curves present CO_2 emissions and global temperature under different carbon taxes when the abatement technology is not available. The dashed curves, present the results with the introduction of a perfect abatement technology in 2100. When the abatement technology is introduced, the flow of CO_2 into the atmosphere drops discontinuously and permanently to zero. The cut in the cumulative carbon dioxide emissions modifies the temperature path, which declines until it reaches a new and much lower steady-state. Figure 35 replicates Figure 14 but includes, in dashed lines, the global average real GDP and welfare effects of the implementation of a carbon tax relative to a scenario with no carbon taxes, when we introduce the abatement technology in 2100. Since the abatement technology eliminates the effect of carbon emission on temperatures, and therefore on amenities and productivity, the deceleration of growth caused by global warming that we observe after 2100 without an abatement technology is now avoided.[23]

H.3. *Clean Energy Subsidies*

At impact, the subsidy on clean energy leads to a reduction in the composite price of energy. Given our Cobb-Douglas production function, the subsidy acts like a positive production subsidy that increases output and encourages innovation, which accelerates growth. Given that the model features dynamic spillovers that are not internalized in equilibrium, such a subsidy is potentially beneficial. Furthermore, the subsidy leads to declines in energy costs that vary across locations. Areas using more clean energy

23. Note that relative real GDP and welfare can be slightly lower in the abatement case for a couple of decades after the invention of the abatement technology. The reason is that the difference in temperatures between the baseline scenario with and without abatement can be larger than the difference in temperature with and without abatement in the scenario with a carbon tax, depending on the second derivative of the temperature function at the time in which the abatement technology arrives. After a few decades, this effect is always dominated by the faster increases in temperature in the case without abatement.

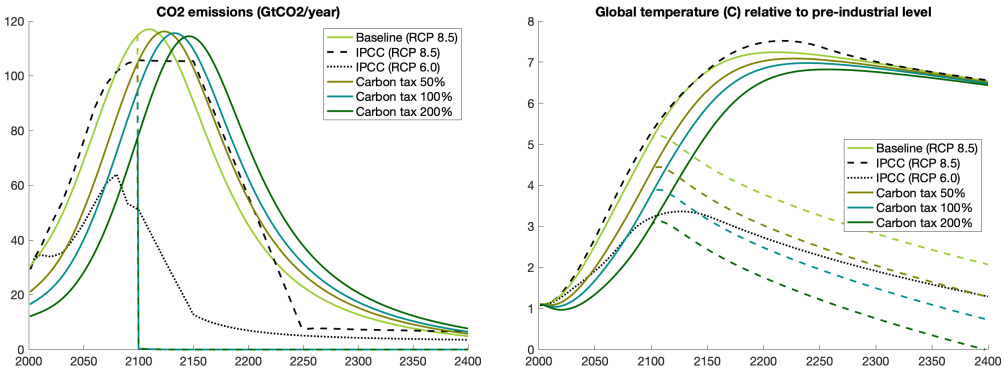

FIGURE 34
CO_2 emissions and global temperature for different carbon taxes with an abatement technology introduced in 2100.

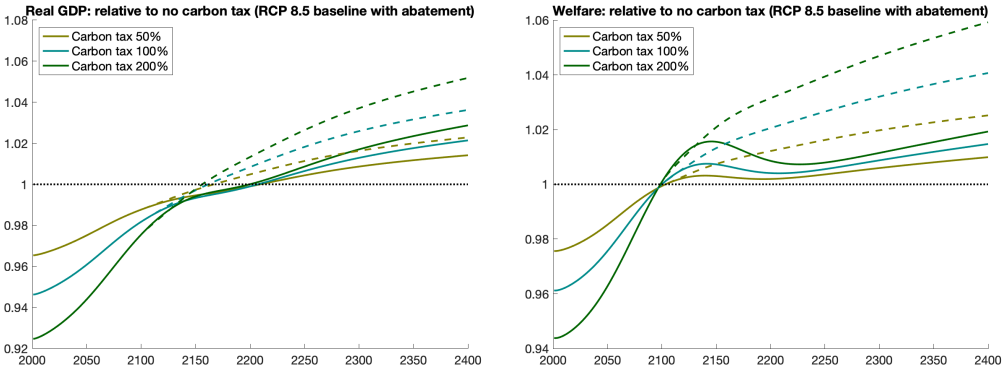

FIGURE 35
Real GDP and welfare for different carbon taxes with an abatement technology introduced in 2100.

relatively to fossil fuels undergo greater declines in the composite price of energy. On average, developed countries tend to be more intensive in clean energy, attracting more households to those places. The relocation of people towards the most productive places rises global real GDP and welfare, but also lowers natality rates and world population in the long-run. A lower population in the Balanced Growth Path leads to lower long-run growth rates. In sum, subsidies increase output and welfare in the short-run, but eventually reduce them in the long-run. As with carbon taxes, the overall economic effects from the subsidy depend on the discount factor. In this case, however, the sign of the short- and long-run effects are reversed relative to the carbon tax. Larger discount factors result in smaller gains. Table 5 presents these results.[24]

24. The result that clean energy subsidies lead to welfare gains despite being ineffective at reducing carbon emissions is related to the literature on interactions between climate policy and pre-existing distortions. Goulder et al. (2016) argues that emissions pricing's advantage over intensity standards (establishment of a floor for the ratio of clean electricity to total electricity) depends importantly on how policies interact with pre-existing distortions, especially with capital. Intensity standards have a

TABLE 5
PDV of real GDP and welfare gains for different clean energy subsidies and discount factors.

	PDV of real GDP			Welfare		
	BGP growth rate	β=0.965	β=0.969	BGP growth rate	β=0.965	β=0.969
s=0% (RCP 8.5 base)	3.076%	1	1	2.971%	1	1
s=25%	3.073%	1.012	1.005	2.967%	1.007	1.003
s=50%	3.066%	1.034	1.008	2.959%	1.021	1.006
s=75%	3.044%	1.098	1.007	2.935%	1.053	1.000

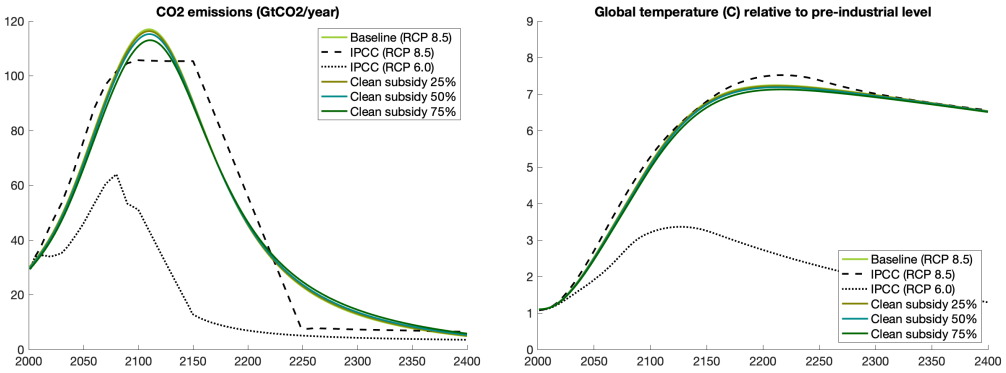

FIGURE 36
CO_2 emissions and global temperature for different clean energy subsidies.

Figure 36 presents the evolution of CO_2 emissions and global temperature for different clean energy subsidies and Figure 37 the spatial distribution of welfare gains from a 75% clean energy subsidy relative to the baseline. The left panel shows the heterogeneous spatial effects from the subsidy. As we discussed above, the subsidy has only a small impact on the temperature path. The main source of spatial heterogeneity comes from the differences in the relative price of fossil fuels and clean energy.[25] Scandinavia has a large relative price of fossil fuels (partly because of other prevailing policies) and so it benefits more from the subsidy than the Arabian peninsula or Australia, where fossil fuels are relatively cheap. Paraguay benefits significantly, since clean energy is cheap there due to the abundance of hydroelectric power. The right panel presents the distribution of welfare gains. Parts of Africa and South America gain in welfare 7%, while some regions in North Africa or the Arabian peninsula gain only 3%. Higher discount factors would make some of these regions lose.

REFERENCES

Allen, T. and C. Arkolakis (2014, 05). Trade and the topography of the spatial economy. *The Quarterly Journal of Economics 129*(3), 1085–1140.

smaller impact on electricity prices and thus on investment, which attenuate existing distortions in capital markets. Parry and Williams III (2012) also finds that emission standards outperform carbon taxes when considering the interactions between climate policies and prior tax distortions.

25. Remember that, in the quantification of our model, we infer this relative price using the relative use of energy sources, which is available at the country level only (which explains the national demarcations in the figure).

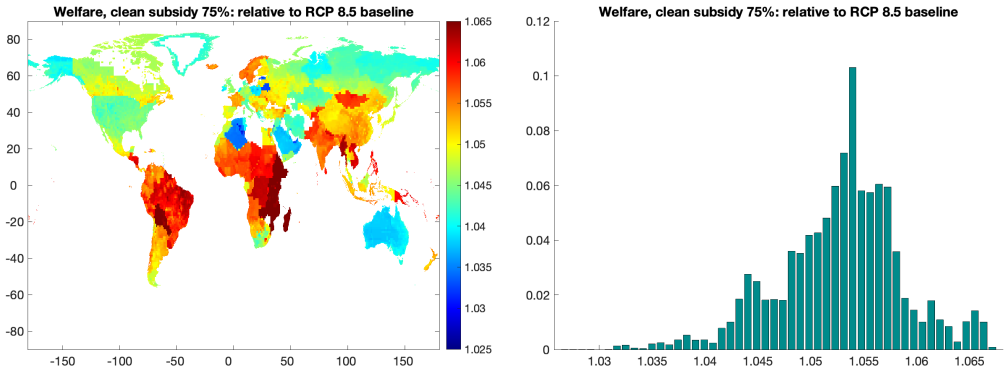

FIGURE 37
Local welfare effects of a clean energy subsidy of 75% with a discount factor of $\beta = 0.965$.

Bauer, N., J. Hilaire, R. J. Brecha, J. Edmonds, K. Jiang, E. Kriegler, H.-H. Rogner, and F. Sferra (2017). Data on fossil fuel availability for shared socioeconomic pathways. *Data in Brief 10*, 44 – 46.

Bernard, A. B., J. Eaton, J. B. Jensen, and S. Kortum (2003, September). Plants and productivity in international trade. *American Economic Review 93*(4), 1268–1290.

Boucher, O. and M. Reddy (2008). Climate trade-off between black carbon and carbon dioxide emissions. *Energy Policy 36*(1), 193–200.

BP (2019). Bp statistical review of world energy.

Carlino, G. A., S. Chatterjee, and R. M. Hunt (2007). Urban density and the rate of invention. *Journal of Urban Economics 61*(3), 389 – 419.

Carrea, L., O. Embury, and C. J. Merchant (2015). Datasets related to in-land water for limnology and remote sensing applications: distance-to-land, distance-to-water, water-body identifier and lake-centre co-ordinates. *Geoscience Data Journal 2*(2), 83–97.

Colella, F., R. Lalive, S. O. Sakalli, and M. Thoenig (2019). Inference with arbitrary clustering.

Conley, T. (1999). Gmm estimation with cross sectional dependence. *Journal of Econometrics 92*(1), 1 – 45.

Conte, B., K. Desmet, D. K. Nagy, and E. Rossi-Hansberg (2021, 09). Local sectoral specialization in a warming world. *Journal of Economic Geography 21*(4), 493–530.

Conte, B., K. Desmet, and E. Rossi-Hansberg (2022, November). On the geographic implications of carbon taxes. Working Paper 30678, National Bureau of Economic Research.

Crippa, M., G. Oreggioni, D. Guizzardi, M. Muntean, E. Schaaf, E. Lo Vullo, E. Solazzo, F. Monforti-Ferrario, J. G. Olivier, and E. Vignati (2019). Fossil co2 and ghg emissions of all world countries. *Publication Office of the European Union: Luxemburg*.

Crippa, M., E. Solazzo, G. Huang, D. Guizzardi, E. Koffi, M. Muntean, C. Schieberle, R. Friedrich, and G. Janssens-Maenhout (2019). High resolution temporal profiles in the emissions database for global atmospheric research (edgar). *Nature Scientific Data*.

Cruz, J.-L. (2021). Global warming and labor market reallocation. *Working Paper*.

Desmet, K., D. Nagy, and E. Rossi-Hansberg (2018). The geography of development. *Journal of Political Economy 126*(3), 903–983.

Desmet, K. and J. Rappaport (2017). The settlement of the United States, 1800–2000: The long transition towards Gibrat's law. *Journal of Urban Economics 98*(C), 50–68.

Desmet, K. and E. Rossi-Hansberg (2015). On the spatial economic impact of global warming. *Journal of Urban Economics 88*(C), 16–37.

Eaton, J. and S. Kortum (2002). Technology, geography, and trade. *Econometrica 70*(5), 1741–1779.

Etminan, M., G. Myhre, E. J. Highwood, and K. P. Shine (2016). Radiative forcing of carbon dioxide, methane, and nitrous oxide: A significant revision of the methane radiative forcing. *Geophysical Research Letters 43*(24), 12,614–12,623.

Forster, P., V. Ramaswamy, P. Artaxo, T. Berntsen, R. Betts, D. Fahey, J. Haywood, J. Lean, D. Lowe, G. Myhre, J. Nganga, R. Prinn, G. Raga, M. Schulz, R. Dorland, G. Bodeker, O. Boucher, W. Collins, T. Conway, and T. Whorf (2007, 10). *Changes in Atmospheric Constituents and in Radiative Forcing.*

Fujino, J., R. Nair, M. Kainuma, T. Masui, and Y. Matsuoka (2006). Multi-gas mitigation analysis on stabilization scenarios using aim global model. *The Energy Journal 27*, 343–353.

Golosov, M., J. Hassler, P. Krusell, and A. Tsyvinski (2014). Optimal taxes on fossil fuel in general equilibrium. *Econometrica 82*(1), 41–88.

Goulder, L. H., M. A. C. Hafstead, and I. Williams, Roberton C. (2016, May). General equilibrium impacts of a federal clean energy standard. *American Economic Journal: Economic Policy 8*(2), 186–218.

Greenwood, J., Z. Hercowitz, and P. Krusell (1997). Long-run implications of investment-specific technological change. *American Economic Review 87*(3), 342–62.

Hastings, D. A., P. K. Dunbar, G. M. Elphingstone, M. Bootz, H. Murakami, H. Maruyama, H. Masaharu, P. Holland, J. Payne, N. A. Bryant, T. L. Logan, J.-P. Muller, G. Schreier, and J. S. MacDonald (1999). The global land one-kilometer base elevation (globe) digital elevation model, version 1.0. *National Oceanic and Atmospheric Administration.*

IEA (2020). Co2 emissions from fuel combustion. Technical report. Database Documentation.

IIASA and FAO (2012). Global agro-ecological zones (gaez v3.0).

IPCC (2013). Climate change 2013: The physical science basis. contribution of working group i to the fifth assessment report of the intergovernmental panel on climate change. *Cambridge University Press.*

Joos, F., R. Roth, J. S. Fuglestvedt, G. P. Peters, I. G. Enting, W. von Bloh, V. Brovkin, E. J. Burke, M. Eby, N. R. Edwards, T. Friedrich, T. L. Frölicher, P. R. Halloran, P. B. Holden, C. Jones, T. Kleinen, F. T. Mackenzie, K. Matsumoto, M. Meinshausen, G.-K. Plattner, A. Reisinger, J. Segschneider, G. Shaffer, M. Steinacher, K. Strassmann, K. Tanaka, A. Timmermann, and A. J. Weaver (2013). Carbon dioxide and climate impulse response functions for the computation of greenhouse gas metrics: a multi-model analysis. *Atmospheric Chemistry and Physics 13*(5), 2793–2825.

Kummu, M., M. Taka, and J. Guillaume (2018, 02). Gridded global datasets for gross domestic product and human development index over 1990–2015. *Scientific Data 5*, 180004.

Monte, F., S. J. Redding, and E. Rossi-Hansberg (2018, December). Commuting, migration, and local employment elasticities. *American Economic Review 108*(12), 3855–90.

Myhre, G., E. J. Highwood, K. P. Shine, and F. Stordal (1998). New estimates of radiative forcing due to well mixed greenhouse gases. *Geophysical Research Letters 25*(14),

2715–2718.
NASA (2009). Nasa ocean biology processing group: Distance to the nearest coast.
NASA (2023). Nasa earth observation.
Nath, I. B. (2020). The food problem and the aggregate productivity consequences of climate change. Technical report, National Bureau of Economic Research.
Nordhaus, W. (2006). Geography and macroeconomics: New data and new findings. *Proceedings of the National Academy of Sciences 103*(10), 3510–3517.
Nordhaus, W. and X. Chen (2016). Global gridded geographically based economic data (g-econ), version 4. *NASA Socioeconomic Data and Applications Center (SEDAC)*.
Papageorgiou, C., M. Saam, and P. Schulte (2017). Substitution between clean and dirty energy inputs: A macroeconomic perspective. *The Review of Economics and Statistics 99*(2), 281–290.
Parry, I. and R. C. Williams III (2012). Moving us climate policy forward: Are carbon taxes the only good alternative? In *Climate Change and Common Sense: Essays in Honour of Tom Schelling*. Oxford Scholarship.
Popp, D. (2004). Entice: endogenous technological change in the dice model of global warming. *Journal of Environmental Economics and Management 48*(1), 742 – 768.
Riahi, K., A. Gruebler, and N. N. (2007). Scenarios of long-term socio-economic and environmental development under climate stabilization. *Technological Forecasting and Social Change 74*, 887–935.
Rogner, H.-H. (1997). An assessment of world hydrocarbon resources. *Annual Review of Energy and the Environment 22*(1), 217–262.
Rohde, R. A. and Z. Hausfather (2020). The berkeley earth land/ocean temperature record. *Earth System Science Data 12*(4), 3469–3479.
Schlenker, W. and M. J. Roberts (2009). Nonlinear temperature effects indicate severe damages to u.s. crop yields under climate change. *Proceedings of the National Academy of Sciences 106*(37), 15594–15598.
Simonovska, I. and M. Waugh (2014). The elasticity of trade: Estimates and evidence. *Journal of International Economics 92*(1), 34–50.
SIO (1977). Archive of geosample data and information from the scripps institution of oceanography geological collections. *NOAA National Centers for Environmental Information*.
UN (2019). *World Population Prospects 2019: Data Booklet*.
Yasuaki, H., Y. Matsuoka, H. Nishimoto, T. Masui, and M. Kainuma (2008). Global ghg emissions scenarios under ghg concentration stabilization targets. *Journal of Global Environmental Engineering 13*, 97–108.